6th European Conference on Computational Mechanics (ECCM 6)
7th European Conference on Computational Fluid Dynamics (ECFD 7)
1115 June 2018, Glasgow, UK

MODELLING HYPERSONIC FLOWS IN THERMOCHEMICAL NONEQUILIBRIUM USING ADAPTIVE MESH REFINEMENT

Chay W. C. Atkins[1], **Ralf Deiterding**[2]

[1] University of Southampton
Faculty of Engineering and the Environment
c.w.atkins@soton.ac.uk

[2] University of Southampton
Faculty of Engineering and the Environment
r.deiterding@soton.ac.uk

Key words: hypersonics, nonequilibirum, AMR

Abstract. Adequate resolution of the flow field is vital to ensure that simulations are sufficiently spatially converged. However, a too finely resolved mesh can lead to excessive computational times. Adaptive Mesh Refinement (AMR) algorithms are able to balance these two constraints by increasing the resolution only where it is needed. In this work, a block-Structured Adaptive Mesh Refinement (SAMR) solver has been coupled to the Mutation++ thermochemical library to enable high resolution simulations of flows in thermochemical nonequilibrium. The solver has been verified using the Method of Manufactured Solutions and computations of hypersonic flows are presented, demonstrating the thermochemical model and the ability of AMR algorithms to resolve flow features.

1 INTRODUCTION

The speeds of hypersonic flight create conditions where thermodynamic relaxation and chemical reactions occur throughout the shock layer, up to the surface of a vehicle. It is vital to account for this thermochemical nonequilibrium in order to obtain an accurate description of the aerothermodynamic environment a hypersonic vehicle experiences.

The two temperature model of Park [1] has been used in a number of solvers that simulate hypersonic flows. The method was implemented in the structured solvers LAURA (Langley Aerothermodynamic Upwind Algorithm) [2] and DPLR (Data Parallel Line Relaxation) [3], and then in unstructured solvers such as US3D (UnStructured 3D) [4] and

LeMANS (The Michigan Aerothermodynamic Navier-Stokes solver) [5]. These have shown that the two temperature model delivers good agreement with experimental results. In this work the model is implemented within a solver that is tightly coupled to an Adaptive Mesh Refinement (AMR) framework.

AMR algorithms aim to minimise the computational cost of simulations by increasing the resolution only where it is needed. The computational framework AMROC (Adaptive Mesh Refinement in Object-oriented C++), implements the Cartesian block-Structured Adaptive Mesh Refinement (SAMR) algorithm of Berger and Colella on parallel computers with distributed memory, where non-Cartesian geometries are considered with an embedded boundary approach [6]. A shock capturing finite volume method has been integrated with the framework to allow highly adaptive simulations of flow fields that include discontinuities.

In previous work [7], a single-temperature TVD-MUSCL scheme for simulating reacting mixtures of thermally perfect gases was developed. In the present work, AMROC has been extended and coupled to the Mutation++ library [8] in order to model flows in thermochemical nonequilibrium using the two temperature model. In addition to the embedded boundary method that was previously implemented, the solver is also able to model non-Cartesian geometries using mapped computational grids, on meshes that are uniform for now.

In Section 2 the governing equations of the thermochemical nonequilibrium model are given. The numerical implementation has been verified using the Method of Manufactured Solutions (MMS), as described in Section 4. Finally, three computations using the AMROC thermochemical nonequilibrium solver are presented in Section 5.

2 GOVERNING EQUATIONS

In the two temperature model, the translational and rotational energies of all species are assumed to be in equilibrium at the translational-rotational temperature T_{tr}. The vibrational and electronic energies of all species are assumed to be in equilibrium at the vibrational-electronic temperature, T_{ve}. Using the two temperature model, the governing equations in Cartesian coordinates for inviscid, two dimensional flow are,

$$\frac{\partial \mathbf{Q}}{\partial t} + \frac{\partial \mathbf{F}}{\partial x} + \frac{\partial \mathbf{G}}{\partial y} = \mathbf{W} \tag{1}$$

where the vector of conserved variables $\mathbf{Q}$, the flux vectors $\mathbf{F}$ and $\mathbf{G}$, and the source vector $\mathbf{W}$ are given by,

$$\mathbf{Q} = \begin{bmatrix} \rho_1 \\ \vdots \\ \rho_{N_s} \\ \rho u \\ \rho v \\ \rho e^{ve} \\ \rho E \end{bmatrix}, \quad \mathbf{F} = \begin{bmatrix} \rho_1 u \\ \vdots \\ \rho_{N_s} u \\ \rho u^2 + p \\ \rho v u \\ \rho e^{ve} u \\ (\rho E + p) u \end{bmatrix}, \quad \mathbf{G} = \begin{bmatrix} \rho_1 v \\ \vdots \\ \rho_{N_s} v \\ \rho u v \\ \rho v^2 + p \\ \rho e^{ve} v \\ (\rho E + p) v \end{bmatrix}, \quad \mathbf{W} = \begin{bmatrix} \dot{w}_1 \\ \vdots \\ \dot{w}_{N_s} \\ 0 \\ 0 \\ Q_{ve} \\ 0 \end{bmatrix}. \tag{2}$$

The thermodynamic state and source terms are calculated using the open source thermochemical library, Mutation++ [8]. The library has been designed to work with high enthalpy flows and contains the functionality to close the governing equations given above. The below equations describe the Mutation++ implementation of the two temperature model for a mixture of neutral species.

The mixture density, ρ, is calculated as the sum of the partial densities, ρ_s,

$$\rho = \sum_{s=1}^{N_s} \rho_s \ , \tag{3}$$

and the pressure, p, is determined using the ideal gas equation and Dalton's Law of partial pressures,

$$p = \sum_{s=1}^{N_s} p_s = \sum_{s} \rho_s \frac{R_u}{M_s} T_{tr} \ , \tag{4}$$

where R_u is the universal gas constant and M_s is the molecular weight of species s. The total energy of the flow is calculated as,

$$E = \sum_{s=1}^{N} \frac{\rho_s}{\rho} e_s + \frac{1}{2} u^2 \ , \tag{5}$$

where the specific internal energy of each species is given by the sum of each of the internal modes and the energy of formation,

$$e_s = e_s^t(T_{tr}) + e_s^r(T_{tr}) + e_s^v(T_{ve}) + e_s^{el}(T_{ve}) + e_s^0 \ . \tag{6}$$

The Rigid-Rotator Harmonic-Oscillator (RRHO) model is used to calculate the internal energies of the molecule. In this model the equations for the internal energy within each mode are derived using a combination of statistical thermodynamics and quantum mechanics [9], giving,

$$e_s^t(T_{tr}) = \frac{3}{2} \frac{R_u}{M_s} (T_{tr} - T_{\text{ref}}) \ , \tag{7}$$

$$e_s^r(T_{tr}) = \begin{cases} \frac{R_u}{M_s}(T_{tr} - T_{\text{ref}}), & \text{for diatomic molecules,} \\ 0, & \text{for atoms,} \end{cases} \tag{8}$$

$$e_s^v(T_{ve}) = \begin{cases} \frac{R_u}{M_s} \frac{\theta_{v,s}}{\exp(\theta_{v,s}/T_{ve})-1}, & \text{for diatomic molecules,} \\ 0, & \text{for atoms,} \end{cases} \tag{9}$$

and

$$e_s^{el}(T_{ve}) = \frac{R_u}{M_s} \frac{\sum_{i=1}^{\infty} g_{i,s}\, \theta_{el,i,s} \exp\left(-\theta_{el,i,s}/T_{ve}\right)}{\sum_{i=1}^{\infty} g_{i,s} \exp\left(-\theta_{el,i,s}/T_{ve}\right)} \ . \tag{10}$$

In these equations, $T_{\text{ref}} = 298.15\,\text{K}$, $\theta_{v,s}$ is the characteristic vibrational temperature of species s and, $g_{i,s}$ and $\theta_{el,i,s}$ are the degeneracy and characteristic electronic temperature, respectively, at energy level i for species s. Although the electronic energy levels are

summed from $i = 1$ to $i = \infty$, only the lower electronic energy levels are usually considered. The large characteristic electronic temperatures of the higher levels mean that they are not excited at the conditions found in hypersonic flows.

The net production rate of a species, $\dot{w}_s$, is calculated as the sum of the species production rate in each reaction,

$$\dot{w}_s = M_s \sum_{r=1}^{N_r} (\beta_{sr} - \alpha_{sr}) \left[k_{f,r} \prod_{i=1}^{N_s} \left(\frac{\rho_i}{M_i} \right)^{\alpha_{ir}} - k_{b,r} \prod_{i=1}^{N_s} \left(\frac{\rho_i}{M_i} \right)^{\beta_{ir}} \right] , \tag{11}$$

where N_r is the number of reactions involving species s, β and α are the stoichiometric coefficients, $k_{f,r}$ is the forward reaction rate and $k_{b,r}$ is the backward reaction rate. The forward reaction rate is found using the Arrhenius equation,

$$k_{f,r}(T_c) = A_{f,r} T_c^{\eta_{f,r}} \exp\left[-\theta_r / T_c\right] , \tag{12}$$

where A_r is the reaction rate constant, θ_r is the activation temperature and $\eta_{f,r}$ is a constant. The rate controlling temperature T_c is determined using Park's two temperature model [1]. The backwards reaction rate is calculated using the forward reaction rate and the equilibrium constant, which is calculated as a function of the Gibbs free energy [8].

The source term used to account for a change in the vibrational-electronic energy is the sum of the translational-vibrational energy exchange and energy changes due to chemical reactions,

$$Q_{ve} = \sum_s Q_s^{T-V} + Q_s^{C-V} + Q_s^{C-el} . \tag{13}$$

The translational-vibrational energy exchange, Q_s^{T-V}, is modelled using a Landau-Teller type equation,

$$Q_s^{T-V} = \rho_s \frac{e_s^v(T_{tr}) - e_s^v}{\tau_{v,s}^{T-V}} , \tag{14}$$

where the vibrational relaxation time is given by the Millikan and White formula, with modified constants [10] and the Park correction time,

$$\tau_{v,s}^{T-V} = \frac{\sum_{r=1}^{N} X_r}{\sum_{r=1}^{N} \frac{X_r}{\tau_{s-r}^{T-V} + \tau_{s-r}^{p}}} . \tag{15}$$

The Millikan and White relaxation time is found using the empirical formula,

$$p\, \tau_{s-r}^{T-V} = \exp\left[A_{s,r} \left(T_{tr}^{-1/3} - B_{s,r} \right) - 18.42 \right] \text{ (in atm-sec)}, \tag{16}$$

and the Park correction time takes the form,

$$\tau_{s-r}^{p} = \sqrt{\frac{\pi k_B \mu_{s,r} T_{tr}}{8 N_A}} \frac{1}{\sigma_s p} . \tag{17}$$

where the collision cross section, σ_s is calculated as,

$$\sigma_s = 3 \text{ x}10^{-21} \left(\frac{50,000}{\min(T_{tr}, 20,000)} \right)^2 . \tag{18}$$

The source terms accounting for change in the vibrational and electronic energy due to chemical reactions, Q_s^{C-V}, Q_s^{C-el}, are given by,

$$Q_s^{C-V} = c_1 \dot{w}_s e_s^v, \quad Q_s^{C-el} = c_1 \dot{w}_s e_s^{el} . \tag{19}$$

In both cases a non-preferential model is used with $c_1 = 1$.

3 NUMERICAL IMPLEMENTATION

In this work, the governing equations for thermochemical nonequilibrium flow have been integrated into the AMROC framework. The solver uses the MUSCL-Hancock scheme [11, 12] and Strang splitting [13] to achieve second order accuracy in both space and time [6]. The reconstruction of variables at the cell faces is carried out by interpolating the primitive variables ρ_s, u, T_{tr} and T_{ve}. The inviscid fluxes are calculated using two temperature versions of the AUSM [14] flux scheme and the van Leer flux vector splitting method [15].

The nonequilibrium solver uses the level set method with ghost cells [6] or the mesh mapping described by LeVeque [16] to model non-Cartesian geometries. 2D axisymmetric flows can be simulated using an axisymmetric source term that takes the form given by Anderson [9].

4 METHOD OF MANUFACTURED SOLUTIONS

The solver was verified using the Method of Manufactured Solutions (MMS). The MMS procedure was first introduced by Roache [17] and is able to verify any code that solves ordinary or partial differential equations [18].

A set of solutions for a two species mixture of O_2 and N_2 was manufactured in terms of the variables ρ_s, u, e_s^{ve} and T_{tr}. These solutions were substituted into Eqs. (3) to (8), to calculate the pressure, mixture density and mixture energies that are used in the governing equations (Eq. (2)). The source terms in the governing equations were replaced by the analytic MMS source term, which was created using the computational algebra package SymPy [19].

The solutions take a similar form to those given by Roy [20],

$$\phi = \phi_0 + \phi_x \sin(a_{\phi,x} \pi x) , \tag{20}$$

and

$$\phi = \phi_0 + \phi_x \cos(a_{\phi,x} \pi x) , \tag{21}$$

and the constants used in each manufactured solution are shown in Table 1. To fully test the flux schemes, two velocity solutions are used to give a supersonic solution and a subsonic solution. The vibrational-electronic energy levels were determined using $T_{ve} \approx$

2000 K. The computational domain stretched between -0.5m $\leq x \leq$ 1.5m and the error between the manufactured solutions and computed results was calculated on four successively finer grids, with a grid refinement ratio of 2.

	ϕ_0	ϕ_x	$a_{\phi,x}$
ρ_{O_2} (kg/m^3)	0.75	0.1	1.0
ρ_N (kg/m^3)	1.0	-0.15	0.5
u (subsonic) (m/s)	600	80	1.5
u (supersonic) (m/s)	1050	100	1.5
$e^{ve}_{O_2}$ (J/kg)	285548	20000	0.75
e^{ve}_{N} (J/kg)	40	5.0	0.75
T_{tr} (K)	1000	200	1.0

Table 1: The constants used in the two temperature MMS tests.

Figure 1 shows the results of the convergence tests when using the van Leer flux scheme. One can see that the scheme is converging at approximately second order accuracy. Similar results were obtained for the subsonic AUSM flux scheme and the results for the supersonic cases are identical for both flux schemes, as expected.

The convergence tests verify both the discretisation of the governing equations, and implementation of the equations of state that were used to derive the analytic source term. Hence, Eqs. (3), (4), (6), (7) and (8), which are implemented in Mutation++, are also verified.

5 SIMULATION RESULTS

5.1 Double Wedge Simulation

A simulation of high enthalpy flow over a double wedge is presented. The simulation is based on the experiment of Pezzella *et al.* [21], where a double wedge was placed into a high enthalpy flow of air. The experimental set up is summarised in Table 2, which gives the wedge geometry and freestream conditions. The geometry is defined by the wedge section lengths, L_1 and L_2, and angles, θ_1 and θ_2.

L_1	θ_1	L_2	θ_2	T_∞	p_∞	U_∞	M_∞	Run time
50.8 mm	30°	25.4 mm	55°	710 K	0.78 kPa	3812 m/s	7.14	242 μs

Table 2: Double wedge geometry and experimental conditions.

A five species mixture of air was used in the simulation, with the reaction rate constants of Park [10]. An initial 200 $\times$ 200 cell mesh was used, with three levels of adaptive mesh refinement and the computation was run on 32 processors. The level set method with ghost cells was used to represent the double wedge geometry, and the fluxes were calculated using the van Leer flux scheme.

Figure 2 shows the density field and mass fraction of atomic oxygen, whilst Fig. 3 shows the level of refinement and the distribution of cells across the available processors.

One can see that the density field is highly resolved at the shock and interaction locations due to the adaptive mesh refinement. Dynamic load balancing is used to distribute the computational cells across the available processors, resulting in areas of high refinement being distributed amongst many processors.

5.2 Lobb Sphere Simulations

The shock standoff distance in hypersonic flows is related to the level of thermochemical nonequilibrium [22]. As such, experiments which measure shock standoff distance from a body travelling at a high velocity can be used to validate nonequilibrium models.

The experimental data of Lobb [22] gives shock standoff distances for half inch diameter spheres travelling between $4,000\,\mathrm{m/s}$ and $6,500\,\mathrm{m/s}$ in air, at four different pressures. Schlieren images were then used to determine the shock standoff distance.

The AMROC solver was used to simulate the experiments conducted with a freestream pressure of $1333\,\mathrm{Pa}$ ($10\,\mathrm{mmHg}$), using a 5 species mixture of air, the Park reaction rate constants and the AUSM flux scheme. In addition to validating the thermochemical model, these simulations were used to verify the axisymmetric source term by using a 2D-axisymmetric computational domain. The ghost fluid method was used to create the sphere and three levels of AMR were used.

A comparison between the simulated and experimental results are shown in Fig. 4 and Table 3, and the thermochemical nonequilibrium is shown in Fig. 5. One can see that the greatest difference between the simulated and experimental shock standoff distances is less than 10% (less than 5% including the experimental error estimates). However, at higher Mach numbers the shock standoff distance is underestimated. The underestimation of the shock standoff distance is identified as a common issue in Park's review of the two temperature model [23]. Park suggests that this may be due to differences between the translational and rotational temperatures, which are not accounted for in the two temperature model.

Mach No.	8.4	11.2	11.6	14.0	14.2	14.8	16.1
Difference (%)	0.98	0.78	5.49	5.23	6.24	5.83	8.48
Err. Diff. (%)	N/A	N/A	4.47	4.02	0.13	3.34	4.51

Table 3: The difference between the simulated and experimental shock standoff distances, with and without the experimental error estimates.

5.3 Mapped Mesh Computation

In this simulation the implementation of the mapped mesh algorithms were verified. A hypersonic flow of nitrogen around a cylinder was simulated using both a mapped mesh and the ghost cell method.

The simulations recreate the experiments of Hornung [24], with the freestream conditions taken from Ref. [25]. The experimental conditions are shown in Table 4.

Cylinder Radius	Mass Frac. N_2	Mass Frac. N	T_∞	p_∞	U_∞	M_∞
0.0127 m	0.927	0.073	1833 K	2.91 kPa	5590 m/s	6.14

Table 4: Cylinder geometry and freestream conditions

In order to transform the computational domain, (ξ, η), to a cylindrical domain, (x, y) the following transformation functions were used:

$$x = \xi \cos(\eta), \quad y = -\xi \sin(\eta). \tag{22}$$

The computational domain was given by $-0.03 \leq \xi \leq -0.0127$ and $0 \leq \eta \leq \pi/2$ in order to create a half inch radius cylinder.

Figure 6 shows a comparison between the mapped mesh simulation and a simulation conducted using the ghost fluid method and two levels of adaptive mesh refinement. The agreement between the two simulations is very good, with the shock shape and standoff being similar. The shock standoff distance on the mapped mesh is approximately 2-3% greater, which could be partly due to more numerical diffusion as the AMR has not been integrated with the mapped mesh. A comparison of computational meshes in the stagnation region is shown in Fig. 7.

6 CONCLUSIONS

The governing equations required to model hypersonic flows have been integrated into the AMROC framework. The source terms and thermodynamic properties of the flow are calculated using the Mutation++ library. The solver has been verified using the Method of Manufactured Solutions and several computations are presented, demonstrating different aspects of the solver and showing good agreement with experimental data.

This work has demonstrated the ability of the AMR solver to produce highly resolved results in regions with complex shock-shock interactions, and shown the two temperature model is able to predict the thermochemical nonequilibrium in hypersonic flows. Future work aims to add viscous fluxes to the solver and couple a near-body mapped mesh with an off-body adaptive mesh using overset algorithms.

REFERENCES

[1] C. Park, *Nonequilibrium Hypersonic Aerothermodynamics*. Wiley-Interscience, 1990.

[2] F. M. Cheatwood and P. A. Gnoffo, "User Manual for the Langley Aerothermodynamic Upwind Relaxation Algorithm (LAURA)," Tech. Rep. April, NASA, 1996.

[3] M. J. Wright, G. V. Candler, and D. Bose, "Data-parallel line relaxation method for the navier-stokes equations," *AIAA journal*, vol. 36, no. 9, pp. 1603–1609, 1998.

[4] I. Nompelis, T. Drayna, and G. Candler, "A parallel unstructured implicit solver for hypersonic reacting flow simulation," in *Parallel Computational Fluid Dynamics 2005*, pp. 389–395, Elsevier, 2006.

[5] L. C. Scalabrin and I. D. Boyd, "Numerical simulation of weakly ionized hypersonic flow for reentry configurations," in *9th AIAA/ASME Joint Thermophysics and Heat Transfer Conference*, no. June, AIAA, 2006.

[6] R. Deiterding, "Block-Structured Adaptive Mesh Refinement- Theory, Implementation and Application," *ESAIM Proceedings*, vol. 34, pp. 97–150, 2011.

[7] R. Deiterding, "A parallel adaptive method for simulating shock-induced combustion with detailed chemical kinetics in complex domains," *Computers & Structures*, vol. 87, pp. 769–783, 2009.

[8] J. B. Scoggins and T. E. Magin, "Development of Mutation++ : MUlticomponent Thermodynamics And Transport properties for IONized gases library in C++," in *11th AIAA/ASME Joint Thermophysics and Heat Transfer Conference*, 2014.

[9] J. D. Anderson, *Hypersonic And High Temperature Gas Dynamics*. AIAA Education Series, second ed., 2006.

[10] C. Park, "Review of chemical-kinetic problems of future NASA missions, I - Earth entries," *Journal of Thermophysics and Heat Transfer*, vol. 7, no. 1, pp. 9–23, 1993.

[11] B. van Leer, "Towards the Ultimate Conservative Difference Scheme. IV. A New Approach to Numerical Convection," *Journal of Computational Physics*, vol. 23, pp. 276–299, 1977.

[12] E. F. Toro, *Riemann solvers and numerical methods for fluid dynamics: a practical introduction*. Springer Science & Business Media, 1999.

[13] G. Strang, "On the construction and comparison of different schemes," *SIAM journal on numerical analysis*, vol. 5, pp. 506–517, 1968.

[14] M.-S. Liou and C. J. Steffen Jr, "A new flux splitting scheme," *Journal of Computational Physics*, vol. 107, pp. 23–39, 1993.

[15] B. van Leer, "Flux Vector Splitting for the Euler Equations," in *Eighth international conference on numerical methods in fluid dynamics*, 1982.

[16] R. LeVeque, "Finite Volume Methods for Hyperbolic Problems," *Cambridge University Press*, vol. 54, p. 258, 2002.

[17] P. J. Roache, "Verification of codes and calculations," *AIAA journal*, vol. 36, no. 5, pp. 696–702, 1998.

[18] K. Salari and P. Knupp, "Code verification by the method of manufactured solutions," tech. rep., Sandia National Labs., Albuquerque, NM (US); Sandia National Labs., Livermore, CA (US), 2000.

[19] A. Meurer, C. P. Smith, M. Paprocki, O. Čertík, S. B. Kirpichev, M. Rocklin, A. Kumar, S. Ivanov, J. K. Moore, S. Singh, T. Rathnayake, S. Vig, B. E. Granger, R. P. Muller, F. Bonazzi, H. Gupta, S. Vats, F. Johansson, F. Pedregosa, M. J. Curry, A. R. Terrel, v. Roučka, A. Saboo, I. Fernando, S. Kulal, R. Cimrman, and A. Scopatz, "Sympy: symbolic computing in python," *PeerJ Computer Science*, vol. 3, p. e103, Jan. 2017.

[20] C. J. Roy, C. Nelson, T. Smith, and C. Ober, "Verification of euler/navier–stokes codes using the method of manufactured solutions," *International Journal for Numerical Methods in Fluids*, vol. 44, no. 6, pp. 599–620, 2004.

[21] G. Pezzella, D. de Rosa, and R. Donelli, "Computational Analysis of Shock Wave Boundary Layer Interactions in Non-equilibrium Hypersonic Flow," *20th AIAA International Space Planes and Hypersonic Systems and Technologies Conference*, no. July, pp. 1–12, 2015.

[22] K. R. Lobb, "Experimental Measurement of Shock Detachment Distance on Spheres Fired in Air at Hypervelocities," *High Temperature Aspects of Hypersonic Flows*, vol. 14, no. 5, pp. 519–527, 1964.

[23] C. Park, "The Limits of Two-Temperature Model," in *48th AIAA Aerospace Sciences Meeting*, no. January, pp. 1–13, 2010.

[24] H. G. Hornung, "Non-equilibrium dissociating nitrogen flow over spheres and circular cylinders," *Journal of Fluid Mechanics*, vol. 53, pp. 149–176, 1972.

[25] G. Tchuen and Y. Burtschell, *Physico - Chemical Modelling in Nonequilibrium Hypersonic Flow Around Blunt Bodies*. 2011.

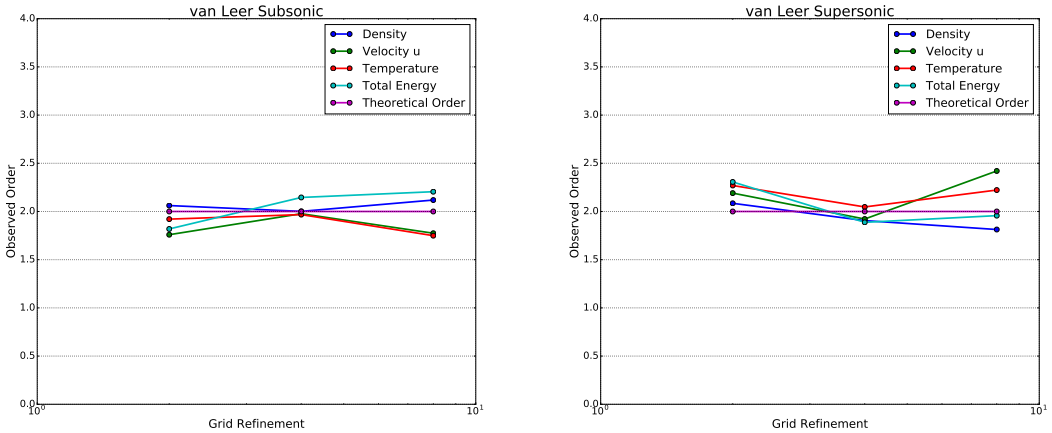

Figure 1: The subsonic (left) and supersonic (right) Method of Manufactured Solutions convergence results, using the van Leer flux scheme.

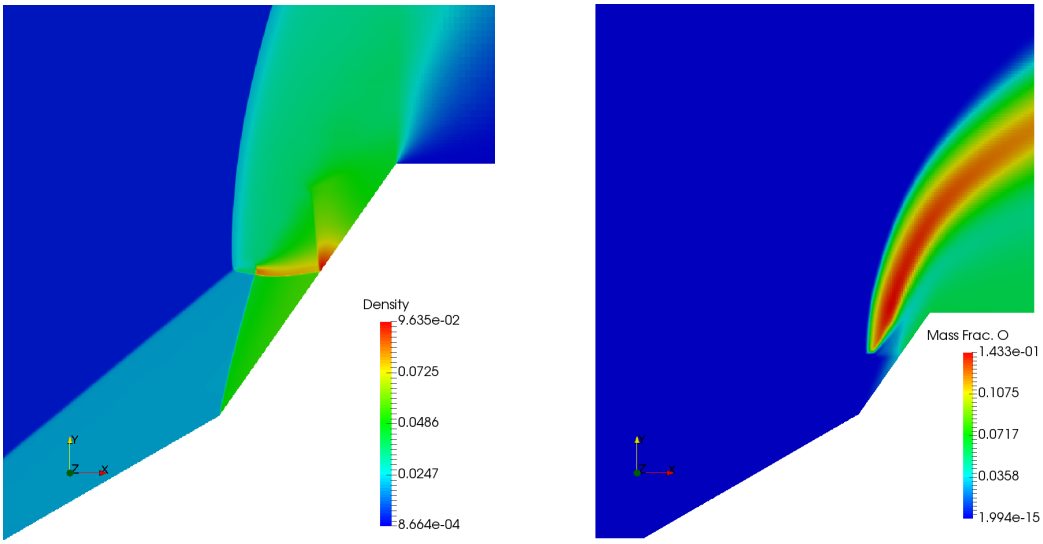

Figure 2: The density field in the shock-shock interaction region (left) and the mass fraction of atomic oxygen (right) in the double wedge simulation.

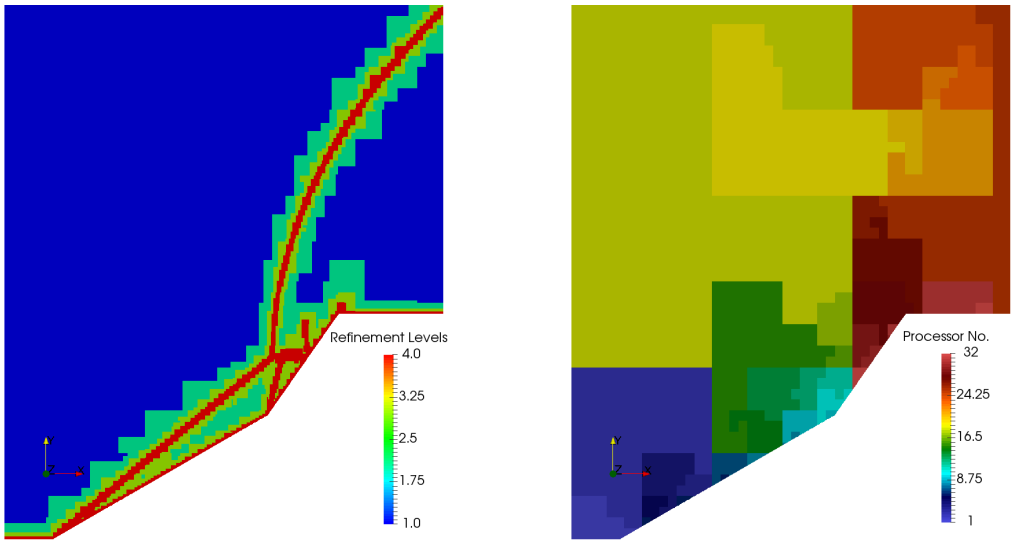

Figure 3: The mesh refinement levels (left) and the parallel distribution (right) in the double wedge simulation.

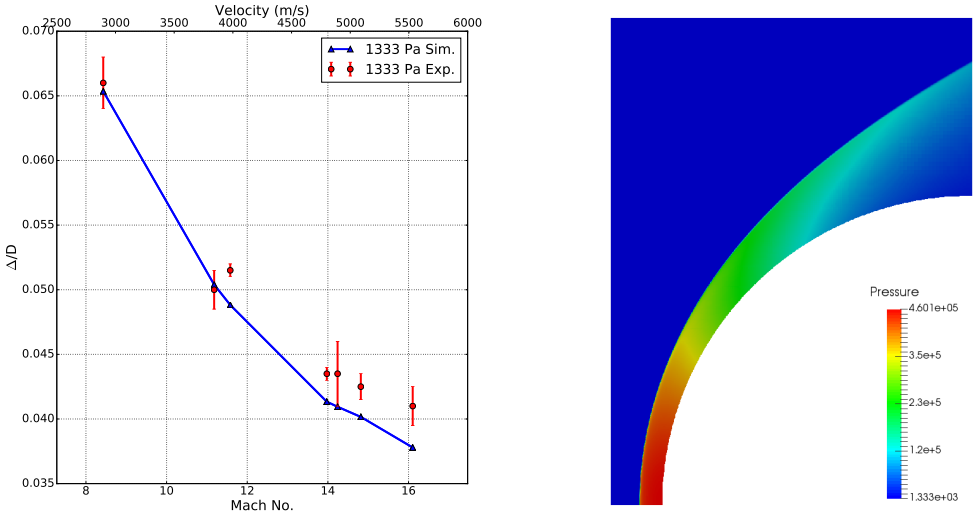

Figure 4: A comparison of the simulated and measured shock standoff distances (left) and an example plot of the pressure field (right). The shock standoff distance (Δ) is normalised by the sphere diameter (D = 0.5 inches).

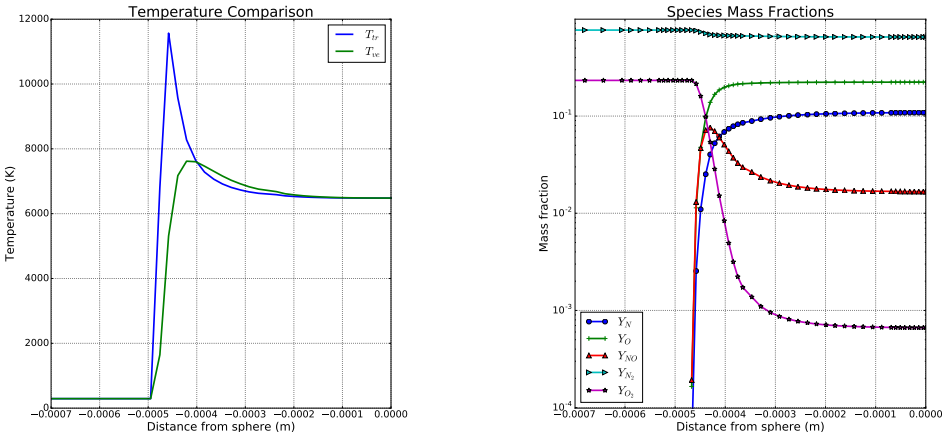

Figure 5: The thermochemical nonequilibrium in the shock layer of the Mach 16.1 simulation.

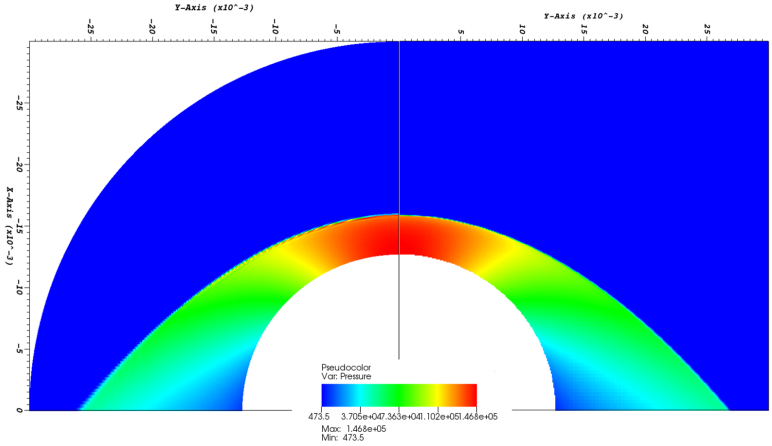

Figure 6: A comparison between the mapped mesh cylinder simulation (left) and the ghost fluid method cylinder simulation (right).

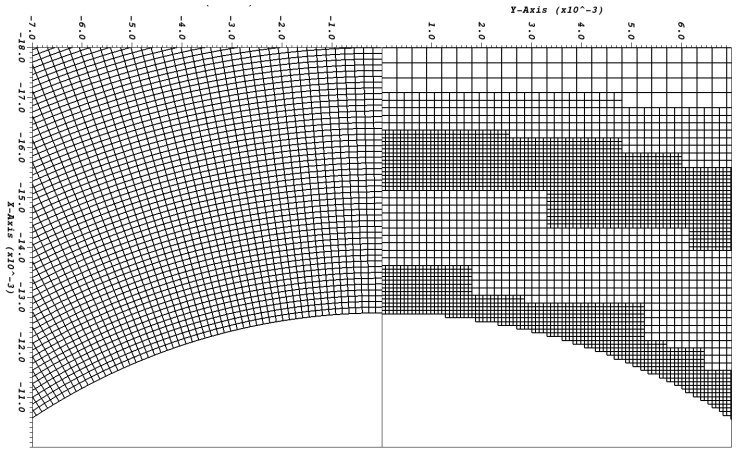

Figure 7: A comparison between the mapped mesh (left) and the refined mesh (right).